Supplementary Information

Fullerene derivative integration controls morphological behaviour and recombination losses in non-fullerene acceptor-based organic solar cells

Apostolos Panagiotopoulos[a1], Kyriakos Almpanidis[a1], Esther Y-H. Hung[b1,b2], Nikolaos Lempesis[c,*], Weidong Xu[d], George Perrakis[e], Sandra Jenatsch[f], Levon Abelian[g], Stoichko Dimitrov[g], Dimitar Kutsarov[a1], Ehsan Rezaee[a1], Benjamin M. Gallant[h1,h2], Vlad Stolojan[a1], Konstantinos Petridis[i], Samuel D. Stranks[d], Henry J. Snaith[b2], George Kakavelakis[i,*] and S. Ravi P. Silva[a1,a2,*]

a1 Advanced Technology Institute, School of Computer Science and Electronic Engineering, University of Surrey, Guildford, UK

a2 Institute for Sustainability, University of Surrey, United Kingdom

b1 MAX IV Laboratory, Lund University, P.O. Box 118, Lund, SE-221 00 Sweden

b2 Clarendon Laboratory, Department of Physics, University of Oxford, Oxford, OX1 3PU, United Kingdom

c Laboratory of Physical Chemistry, Department of Chemistry, University of Ioannina, Ioannina 45110, Greece

d Department of Chemical Engineering and Biotechnology, University of Cambridge, Philippa Fawcett Drive, Cambridge CB3 0AS, UK

e Institute of Electronic Structure and Laser (IESL), Foundation for Research and Technology – Hellas (FORTH), 70013 Heraklion, Crete, Greece

f Fluxim AG, Katharina-Sulzer-Platz 2, 8406 Winterthur, Switzerland

g School of Physical and Chemical Sciences, Queen Mary University of London, London E1 4NS, U.K.

h1 School of Chemistry, University of Birmingham, Edgbaston, Birmingham, B15 2TT, United Kingdom

h2 Department of Solution-Processing of Hybrid Materials and Devices Helmholtz-Zentrum Berlin für Materialien und Energie GmbH, Kekuléstraße 5, 12489 Berlin, Germany

i Department of Electronic Engineering, School of Engineering, Hellenic Mediterranean University, Romanou 3, Chalepa, Chania, Crete, Greece

Corresponding authors: s.silva@surrey.ac.uk, nlempesis@uoi.gr, kakavelakis@hmu.gr

Full chemical names

[6,6]-Phenyl-C71-butyric acid methyl ester ($PC_{71}BM$)

Poly[(2,6-(4,8-bis(5-(2-ethylhexyl)-4-fluorothiophen-2-yl)-benzo[1,2-b:4,5-b']dithiophene))-alt-(5,5-(1',3'-di-2-thienyl-5',7'-bis(2-ethylhexyl)benzo[1',2'-c:4',5'-c']dithiophene-4,8-dione))] (PM6).

2,2'-((2Z,2'Z)-((12,13-bis(2-ethylhexyl)-3,9-diundecyl-12,13-dihydro-[1,2,5]thiadiazolo[3,4-e]thieno[2",3'':4',5']thieno[2',3':4,5]pyrrolo[3,2-g]thieno[2',3':4,5]thieno[3,2-b]indole-2,10-diyl)bis(methanylylidene))bis(5,6-difluoro-3-oxo-2,3-dihydro-1H-indene-2,1-diylidene)) (Y6).

2,2'-((2Z,2'Z)-((12,13-bis(2-ethylhexyl)-3,9-(2-butyloctyl)-12,13-dihydro [1,2,5]thiadiazolo [3,4-e]thieno[2",3'':4',5']thieno[2',3':4,5]pyrrolo[3,2-g]thieno [2',3':4,5]thieno[3,2-b]indole-2,10-diyl)bis(methanylylidene))bis(5,6-difluoro-3-oxo-2,3-dihydro-1H-indene-2,1-diylidene))dimalononitrile (L8BO).

[6,6]-phenyl-C61-butyric acid methyl ester ($PC_{61}BM$).

[6,6]-phenyl-C61-butyric acid hexyl ester (PCBC6).

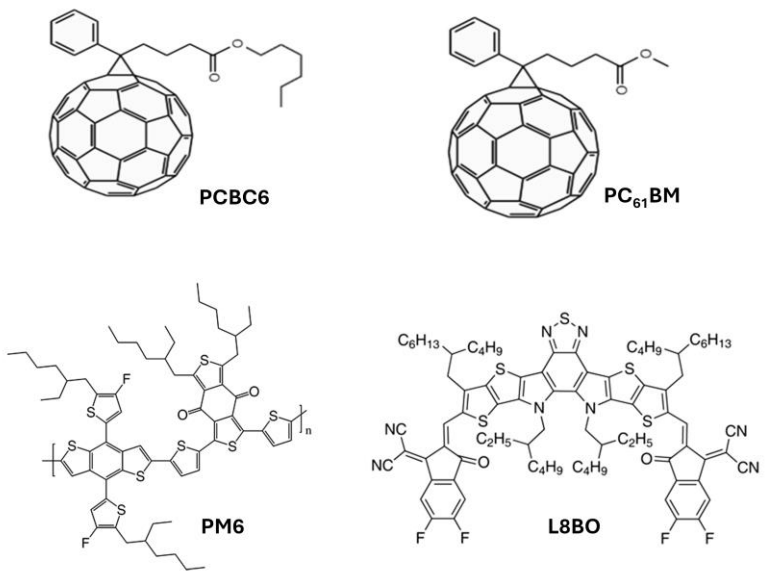

Figure S1. Chemical structures of donor and acceptors used for the binary and ternary blends.

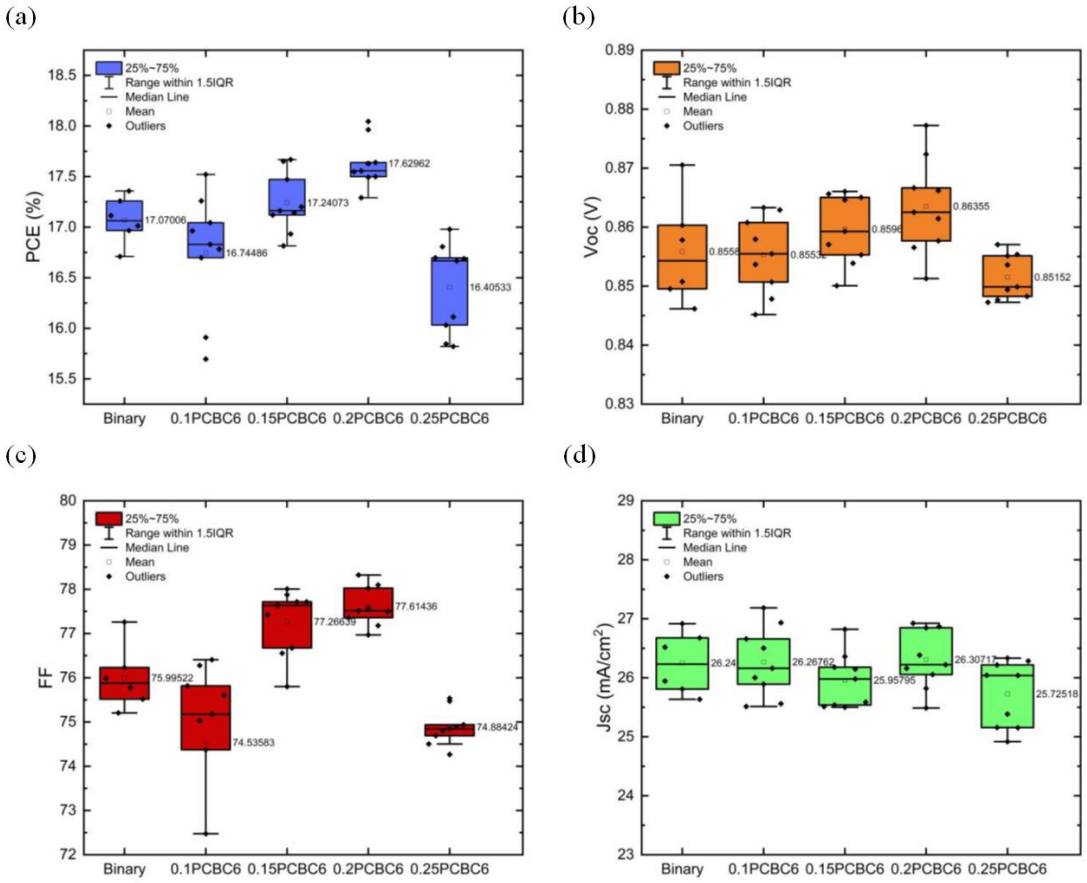

Figure S2. PCBC6 ternary cells optimization statistical analysis (a) PCE, (b) V_{oc}, (c) FF and (d) J_{sc}.

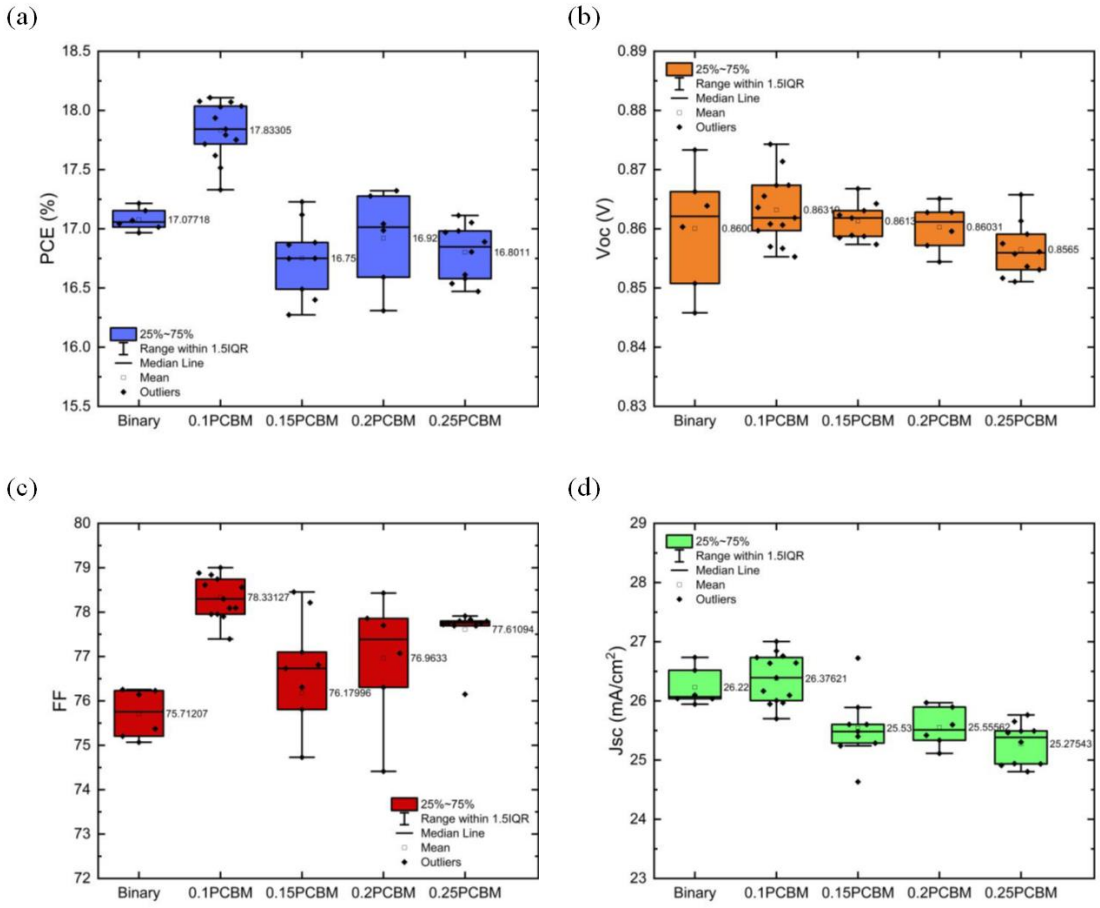

Figure S3. $PC_{61}BM$ ternary cells optimization statistical analysis (a) PCE, (b) V_{oc}, (c) FF and (d) J_{sc}.

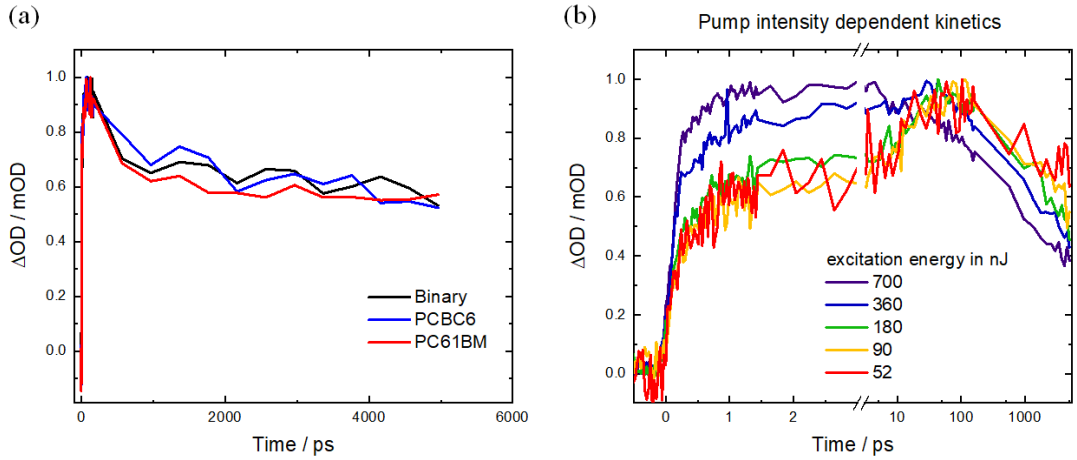

Figure S4. (a) Transient absorption signal at 631 nm (PM6 bleach) and 800 nm excitation (at L8BO) in PM6:L8BO and PM6:L8BO: fullerene samples, (b) Excitation intensity dependent transient absorption at 631 nm (PM6 bleach) and 800 nm excitation (at L8BO) in PM6:L8BO and PM6:L8BO: fullerene samples.

Device Simulations Part A (C-V)

To obtain the simulated $1/C^2$–V curves (see Figure 4(d)), we performed steady-state device simulations (COMSOL Multiphysics) including optical full-wave electromagnetic modelling and electrical drift-diffusion modelling based on the Finite Element Method [1,2].

Specifically, optical simulations (see Figure S5(a), SI) provided spatially resolved charge carrier generation profiles, which were coupled into the electrical model to solve the steady-state Poisson and continuity equations at a series of applied DC biases. In this work, we assume a sufficiently high driving force for exciton dissociation into free charge carriers [3], considering also that explicitly modeling exciton diffusion and dissociation in polymer and acceptor domains remains challenging and beyond the scope of this analysis. Moreover, the device performance is studied by considering Shockley–Read–Hall (SRH) and bimolecular recombination [4].

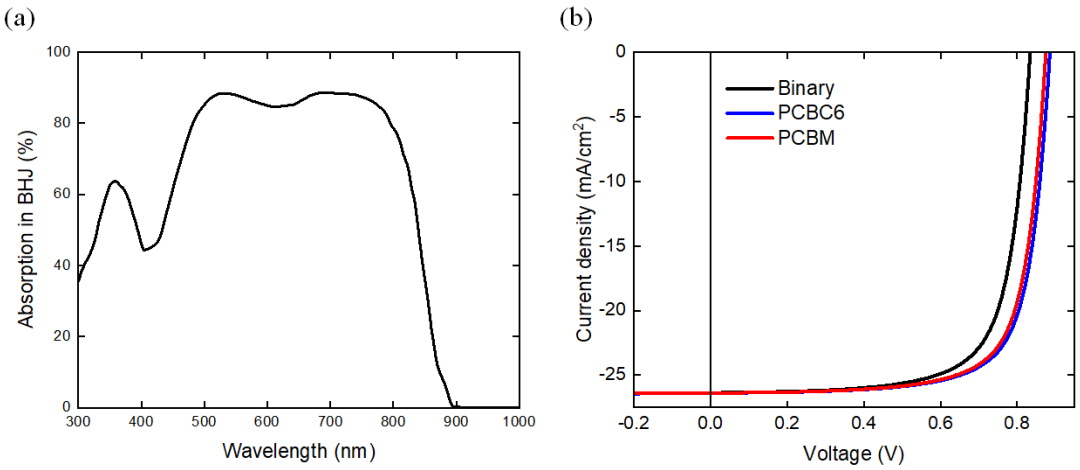

Figure S5. Simulated (a) absorption in BHJ active layer and (b) J–V curves for binary (black), and ternary PCBC6 (blue) and PCBM (red) OSCs.

From the simulated electron-hole carrier distributions, the space charge density was calculated as $\rho = q(p - n + N_D - N_A)$ [5], where q is the elementary charge, p and n are the hole and electron concentrations, and ND and NA are the donor and acceptor doping densities, respectively. The total charge was then calculated as $Q = \int \rho(x)dx$, integrated over the active

layer [5]. The capacitance was derived by numerically differentiating the charge with respect to the applied voltage, enabling the construction of the simulated $1/C^2$–V characteristics under the quasi-static approximation [6].

The device structure modeled was ITO/PEDOT:PSS/BHJ/PNDIT-F3N/Ag (see also inset in Figure 3(a), where indium-tin-oxide (ITO) and silver (Ag) serve as transparent and back electrodes, respectively. Poly(ethylenedioxythiophene):poly-(styrene sulfonate) (PEDOT:PSS) and PNDIT-F3N form the hole-transporting layer (HTL) and electron-transporting layer (ETL), respectively. BHJ denotes either binary or ternary bulk heterojunction active layers. The complex refractive indices used in the optical modelling were obtained from refs [4,7,8]. Material parameters used in the electrical modelling for the binary and ternary blends are listed in Table S1 (SI) and were obtained from ref [4]. Moreover, the effective LUMO levels for each blend were extracted by fitting the simulated $1/C^2$ characteristics to the experimental. The resulting values and trends in effective LUMO levels and band gaps are consistent with theoretical and experimental studies, that is shallower for ternary devices (see Table S1, SI) [9]. Moreover, simulated $1/C^2$ curves show close agreement with experimental results when changing the blend. Corresponding simulated J–V characteristics (Figure S5.(b), SI) also reproduce the experimentally observed V_{oc} trend, with ternary OSCs exhibiting higher open-circuit voltages than the binary devices (slightly higher for PCBC6 than PCBM; see Table 1). These results further support the interpretation that fullerene energetics play a key role in tuning both V_{bi} and V_{oc} in these systems [10].

Table S1: Material parameters used in the device simulation for C-V analysis.

Parameters	**PM6:L8-BO**	**PM6:L8-BO:PCBC6**	**PM6:L8-BO:$PC_{61}BM$**
Dielectric permittivity	3	3	3
CB density of states (m^{-3})	1×10^{26}	1×10^{26}	1×10^{26}
VB density of states (m^{-3})	1×10^{26}	1×10^{26}	1×10^{26}
Electron affinity (eV)	3.9 (fitting)	3.84 (fitting)	3.85 (fitting)

Effective band gap (eV)	1.25 (LUMO–HOMO (donor))	1.31 (LUMO–HOMO (donor))	1.30 (LUMO–HOMO (donor))
Thickness (nm)	120	120	120
Electron-hole mobility ($cm^2/V{\cdot}s$)	1.5×10^{-3}	1.5×10^{-3}	1.5×10^{-3}
Free to free charge recombination coefficient (m^3/s)	1.77×10^{-17}	1.77×10^{-17}	1.77×10^{-17}
SRH electron-hole lifetime (μs)	8.62 (exp.)	9.04 (exp.)	8.82 (exp.)
Doping level (cm^{-3})	1.5×10^{16}	1.5×10^{16}	1.5×10^{16}

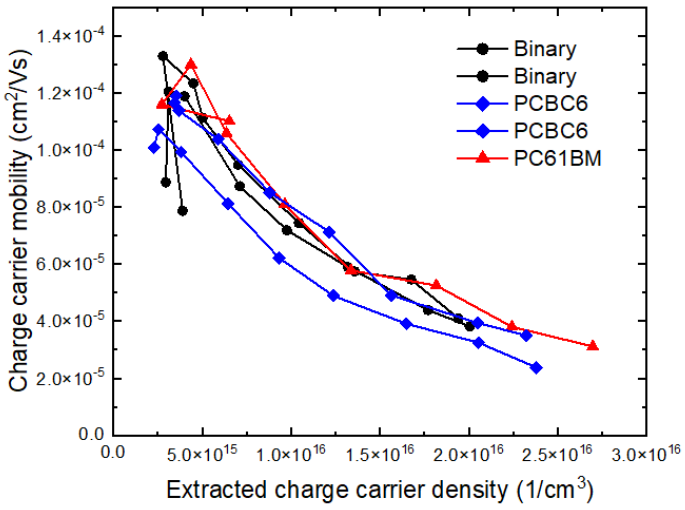

Figure S6. Extracted charge carrier mobility from photo-CELIV as a function of extracted charge density (illumination intensity).

Device Simulations Part B (Steady-state and transient)

Full electro-optical device simulations in this section were performed with Setfos version 5.5 (www.fluxim.com/setfos-intro). The goal was not to obtain a quantitative fit of the measurement but to reproduce the experimental trends seen in measurements on OPV devices. Thus, the model was chosen as simple as possible but as complex as necessary. Figure S7 shows

the simulated device stack and the energy level diagram. Table S2 lists the input parameters for simulation results shown in Figure S8. The parameters modified between the 3 models (SRH lifetime and electron mobility of the absorber layer) are highlighted in bold.

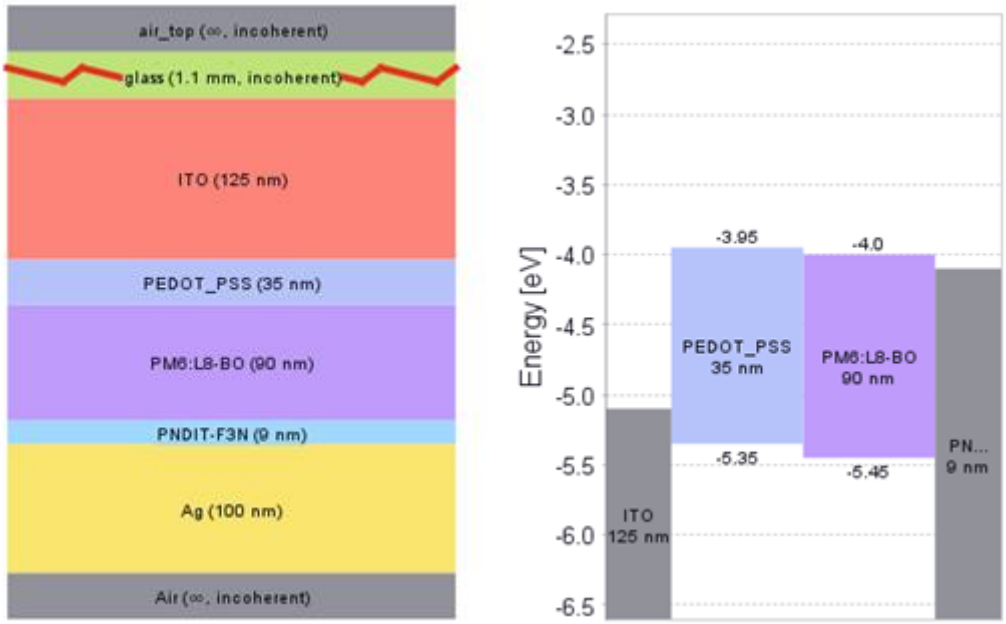

Figure S7: Device stack (left) and energy level diagram (right) used for electro-optical device simulation in Setfos.

Table S2: Electrical material parameters used in the device simulation for steady-state and transient analysis. Changes in the three models (Figure S8) are highlighted in **bold**.

Parameters	**PEDOT:PSS (identical for all 3 models)**	**Binary**	**Ternary**	**Increased mobility alternative**
Dielectric permittivity	3.5	3.5	3.5	3.5
HOMO/LUMO density of states (m^{-3})	1×10^{27}	1.5×10^{27}	1.5×10^{27}	1.5×10^{27}
HOMO / LUMO energy (eV)	5.35 / 3.95	5.45 / 4.0	5.45 / 4.0	5.45 / 4.0

Electron mobility ($cm^2/V·s$)	1×10^{-4}	1×10^{-3}	1×10^{-3}	1×10^{-3}
Hole mobility ($cm^2/V·s$)	1×10^{-3}	**1.2×10^{-4}**	**1.2×10^{-4}**	**6×10^{-4}**
Langevin prefactor	1	1×10^{-3}	1×10^{-3}	1×10^{-3}
SRH electron-hole lifetime (μs)	-	**10**	-	**10**
Acceptor doping level (cm^{-3})	1×10^{18}	-	-	-

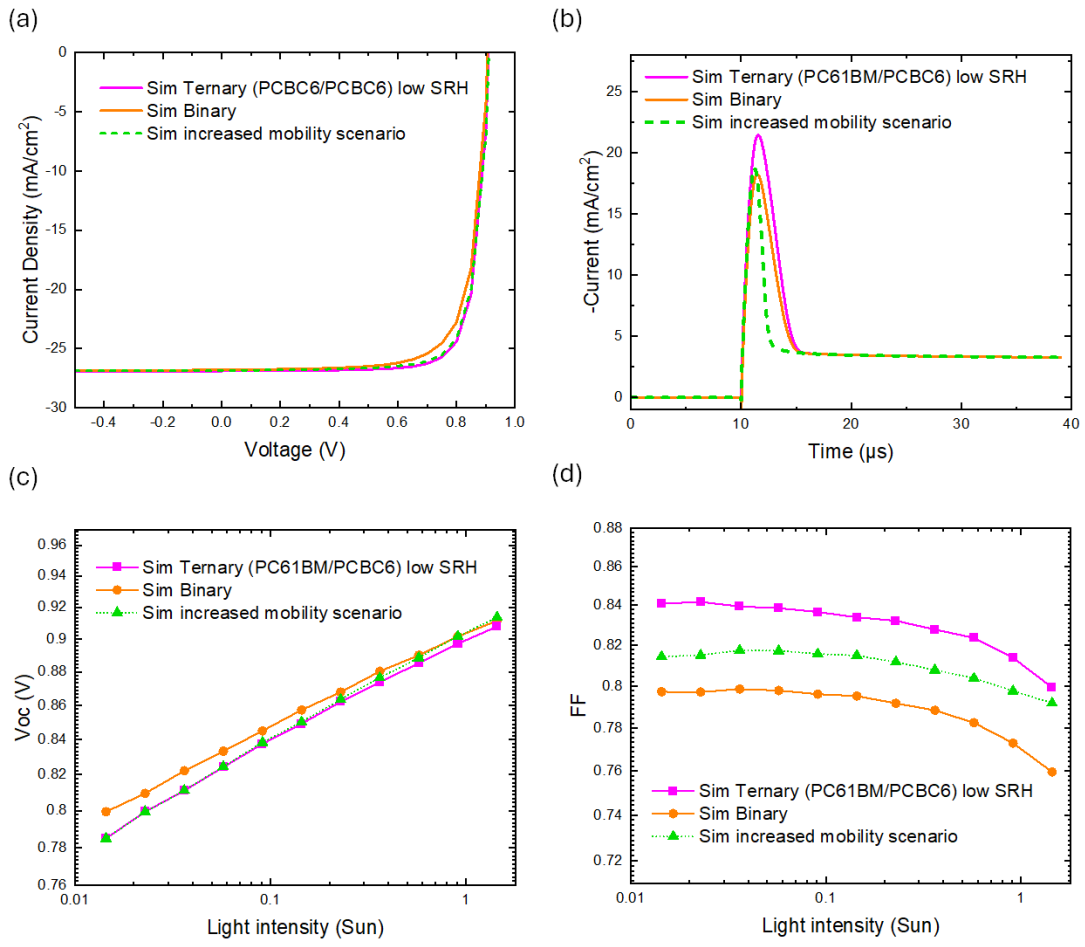

Figure S8. (a) J-V device simulation with/without SRH recombination and same data with an increased hole mobility with respect to the binary model, (b) simulated photo-CELIV for the same 3 model parameter sets, (c) Simulated Voc and (d) FF vs. light intensity trend for the 3 cases.

Table S3: Comparative summary table of recent ternary OSCs

Active layer	**Third component**	**V_{oc} (V)**	**J_{sc} (mA/cm^2)**	**FF**	**PCE (%)**	**Stability protocol / time**	**Year/ Ref.**
PM6:L8-BO	**PCBC6**	**0.87**	**26.85**	**78.7**	**18.38**	**100 mW/cm^2 T_{82} = 525 h**	**This study**
PM6:L8-BO	**$PC_{61}BM$**	**0.86**	**26.55**	**78**	**18.10**	**100 mW/cm^2 T_{85} = 525 h**	**This study**
PM6:L8-BO	Pt1	0.90	27.56	77.60	19.24	100 mW/cm^2 T_{80} = 1270 h (extrapolated)	2025/[11]
PM6:eC9-4F	T10	0.873	28.26	80.68	19.91	100 mW/cm^2 T_{80} = 1609 h	2025/[12]
PM6:Y6	ITOA	0.87	27.57	77.63	18.62	100 mW/cm^2 144h	2024/[13]
PM6:D18	b-PYIT-10	0.944	23.27	67.74	14.89	100 mW/cm^2 T_{90} = ~ 520 h	2024/[14]
PM6:BTP-eC9	isoIDTIC	0.866	27.30	80.4	19.0	100 mW/cm^2/ T_{80} = 254 h	2023/[15]
PM6:Y6	dT9TBO	0.88	27.17	77.26	18.41	100 mW/cm^2 T_{80} = 500 h	2023/[16]

PM6:L8-BO	D18	0.896	26.7	81.9	19.6	100 mW/cm^2 $T_{77.8}$ = 350 h	2022/[4]
PM6: BTP-eC9	$PC_{71}BM$	0.856	26.93	79.4	18.3	100 mW/cm^2 T_{80} = 3 h	2020/[17]
PM6:Y6	O-IDTBR	0.85	25.75	76	16.6	100 mW/cm^2 225 h	2020/[18]

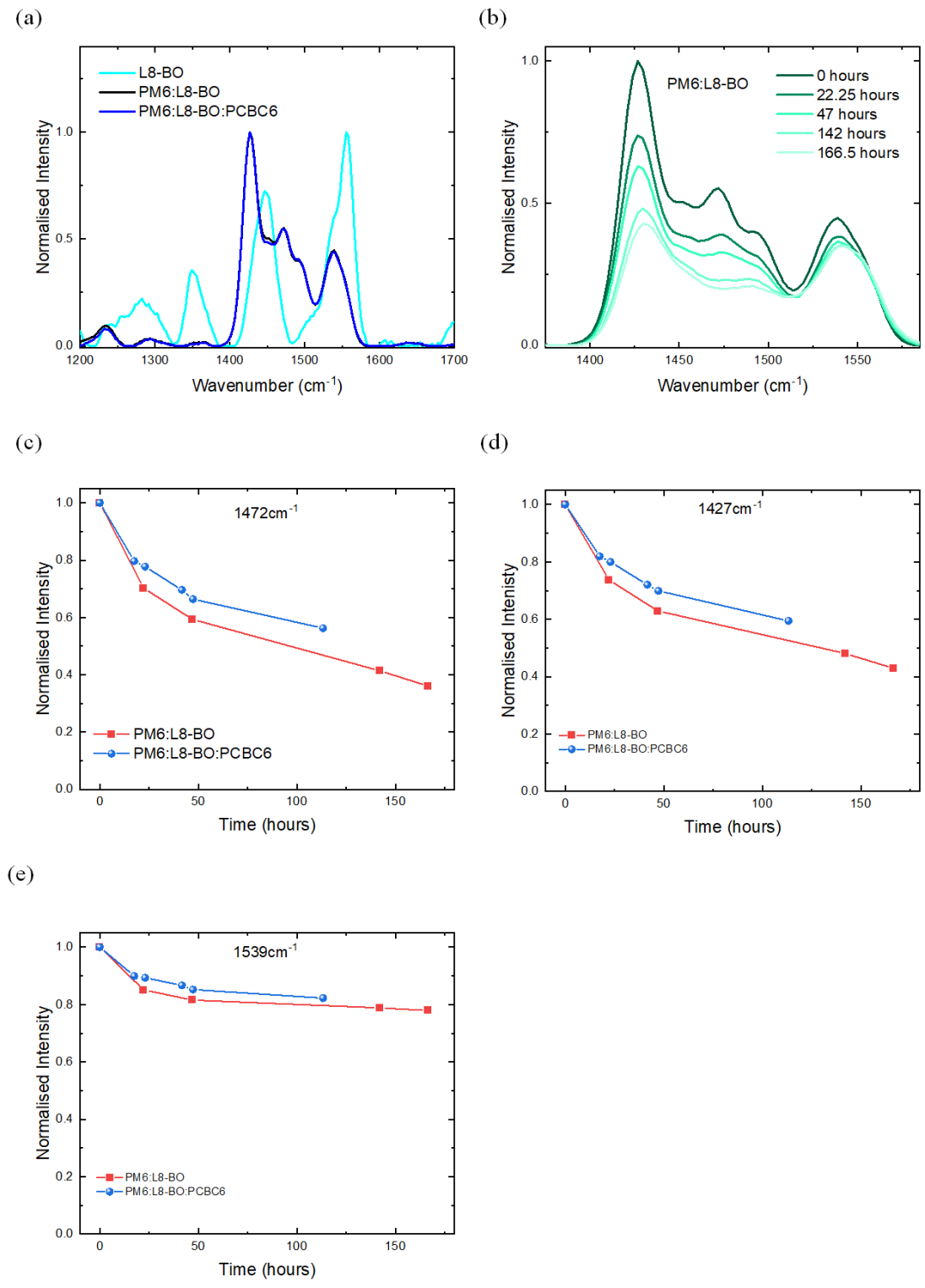

Figure S9. (a) Raman spectra of undegraded films, (b) Zoomed view of the light-induced degradation in the neat PM6:L8-BO film, (c)-(d) Kinetic of normalized intensity decay for the peak corresponding at 1472 cm^{-1}, 1427 cm^{-1}, 1539 cm^{-1}, respectively.

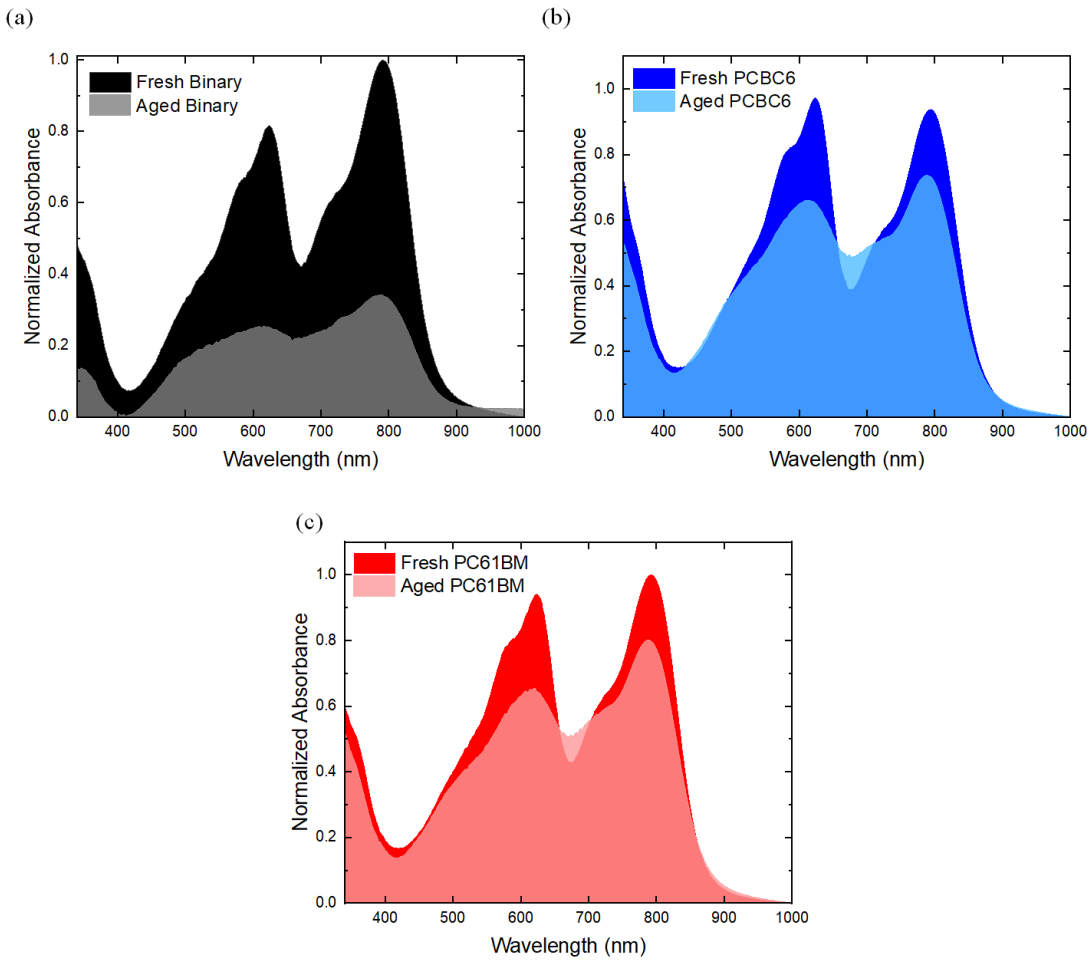

Figure S10. Comparison of absorption changes of (a) PM6:L8-BO, (b) PM6:L8-BO:PCBC6, (c) PM6:L8-BO:PCBM fresh and aged films.

Model system's setup

Three model systems were built. The first one, henceforth called system 1, corresponded to the binary PM6:L8-BO system, whereas the other two systems, hereafter called system 2 and 3, respectively, corresponded to the two ternary systems, PM6:L8-BO:PCBC6 and PM6:L8-BO:$PC_{61}BM$, respectively. All built model systems complied fully with the compositional requirements characterizing their experimental counterparts. All relevant details are included in Table S4.

Table S4: Compositional details of the three model systems used in this work

System ID	Components	Molecular ratio
System 1	PM6 + L8BO	1 : 1.2
System 2	PM6 + L8BO + PCBC6	1 : 1 : 0.2

System 3	PM6 + L8BO + $PC_{61}BM$	1 : 1.1 : 0.1

To represent accurately a polymer such as PM6, whose average molecular weight was reported to be between 30 and 35 kDa, a value of about 33 kDa was selected. Given that the PM6 monomer molecular weight is 1220.9 Da, totally 27 monomers were included per simulated polymer chain. In our analysis, a total of four PM6 chains were considered for a total of 108 PM6 monomers. Based on that and the experimental molecular ratio reported in Table S4, the number of molecules of all other constituents were then calculated and is reported in Table S5. The initial configurations of all simulated systems were then built with the help of Packmol ensuring a random insertion of all constituent parts into a cubic simulation box.[19]

Table S5: Details on the molecular composition of all simulated model systems

System ID	# of PM6 chains	# of PM6 monomers	# L8BO molecules	# PCBC6 molecules	# PC61BM molecules
System 1	4	108	130	-	-
System 2	4	108	108	22	-
System 3	4	108	119	-	11

For the estimation of the volumetric thermal expansion coefficient α_v (Eq. S1), two more systems were built: a system of a) pure amorphous PM6 and b) pure amorphous L8-BO. For the creation of the initial configurations of both systems, Packmol was used.

Classical molecular dynamics (MD) simulations:

Classical MD simulations were performed with the LAMMPS package [20]. The equations of motion were integrated using Velocity-Verlet with a 1 fs time step [21]. To maintain isothermal conditions, the deterministic Nosé-Hoover thermostat with a time constant of 0.1ps was used [22,23]. Periodic boundary conditions were applied all three directions of the simulated bulk systems. The sampling process took place every 500 fs for the computation of ensemble averages, whereas a snapshot of the trajectory was taken every 1000 fs for visualization purposes. Interatomic interactions for all components (PM6, L8-BO, PCBC6 and PC61BM)

were described by the OPLS all-atom force-field using LigParGen.[24] Typical Lorentz-Berthelot mixing rules [25] were applied for non-bonded interactions between dissimilar atoms. The van der Waals and electrostatic non-bonded interactions were calculated using a real-space cutoff radius of 10 Å and 8 Å, respectively, whereas the particle-particle-particle-mesh (PPPM) scheme[26] with an accuracy of 0.0001 (kcal/mol)/Å was used for the consideration of long-range electrostatic interactions.

The initial configurations of all simulated systems were obtained using Packmol by randomly positioning all components at the experimentally prescribed concentration into the simulation box [19]. The initial structures were thoroughly equilibrated at 300 K and 1 atm during a 20 ns long simulation in the isobaric-isothermal NPT statistical ensemble, where the number of atoms N, the system's pressure P and the temperature T were kept constant, allowing for the simulation box edge vectors to change freely and independently and assume their equilibrium length. Proper and adequate equilibration was ensured by monitoring the system's potential energy and density. For the computation of the thermal expansion coefficient α_v, by virtue of Eq. S1, each system was equilibrated based on the simulation protocol described above, at seven relevant temperatures spanning 300 to 450K with a 25K temperature step and constant pressure 1 atm. The thermal expansion coefficient was then computed from the slope of a linear fit passing through the simulated points of the equilibrium system's volume versus temperature divided by the system's initial volume V_0 at 300K.

$$a_v = \frac{1}{V_0}\left(\frac{\partial V}{\partial T}\right)_P \quad \text{Eq. S1}$$

Self-diffusion coefficients, D, of water molecules were calculated by MD simulations in the NPT statistical ensemble and by virtue of Eq. S2 from the intercept of the mean squared displacement (MSD) when plotted against time in a doubly logarithmic plot [27].

$$D = \lim_{t\to\infty} \frac{MSD}{2dt} \quad \text{Eq. S2}$$

Where, d is the dimensionality of the space where diffusion is monitored. For the total diffusion coefficient considering diffusion in three-dimensional space, d = 3. The MSD was calculated with the help of Eq. S3 for the center of mass of all fullerene molecules (i.e., PCBC6 or $PC_{61}BM$) in all three directions. To enhance statistics, averaging, indicated in Eq. S3 by angular brackets, took place over the entire ensemble of molecules and over multiple time origins. In Eq. S3, **r** is the position vector of the center of mass of all considered N fullerene molecules.

$$MSD = \langle (\boldsymbol{r}(t) - \boldsymbol{r}(0))^2 \rangle = \frac{1}{N}\sum_{i=1}^{N}(\boldsymbol{r}_i(t) - \boldsymbol{r}_i(0)^2) \quad \text{Eq. S3}$$

To gain insight into each system's homogeneity and uniform distribution of molecules therein during the MD simulations, the system's gyration tensor **S** was employed. For a system comprising N molecules (of similar or dissimilar type), the system's gyration tensor **S** [28] is given by Eq. S4, where x_i, y_i and z_i are the position vector elements of atom i and x_{cm}, y_{cm} and z_{cm} are those of the center of mass of the system. Having calculated the time averaged **S**, sampled every 500 fs, for every system, various shape descriptors can be derived, such as the relative shape anisotropy k (second invariant) and the asphericity b measuring the deviation from spherical symmetry. Here, we chose to focus on k and b enclosing information on the degree of homogeneity of each system.

$$S = \frac{1}{N}\begin{pmatrix} \sum_i (x_i - x_{cm})^2 & \sum_i (x_i - x_{cm})(y_i - y_{cm}) & \sum_i (x_i - x_{cm})(z_i - z_{cm}) \\ \sum_i (x_i - x_{cm})(y_i - y_{cm}) & \sum_i (y_i - y_{cm})^2 & \sum_i (y_i - y_{cm})(z_i - z_{cm}) \\ \sum_i (x_i - x_{cm})(z_i - z_{cm}) & \sum_i (y_i - y_{cm})(z_i - z_{cm}) & \sum_i (z_i - z_{cm})^2 \end{pmatrix} \quad \text{Eq. S4}$$

In particular, asphericity b, computed with the help of Eq. S5, is a measure of how far we are from a distribution of atoms/molecules within a perfect sphere, where all atoms and molecules are distributed uniformly. Small values of b indicate a uniform distribution of atoms/molecules. Similarly, relative anisotropy k, as computed via Eq. S6, is an additional measure of uniform distribution of atoms/molecules. The smaller k is, the more spherically symmetric and thus homogeneously distributed atoms/molecules are.

$$b = \lambda_z - \frac{1}{2}(\lambda_y + \lambda_x) \quad \text{Eq. S5}$$

$$k = \frac{3}{2}\frac{\lambda_x^2 + \lambda_y^2 + \lambda_z^2}{(\lambda_x + \lambda_y + \lambda_z)^2} - \frac{1}{2} \quad \text{Eq. S6}$$

where λ_x, λ_y and λ_z are the three eigenvalues of **S** with $\lambda_x \leq \lambda_y \leq \lambda_z$.

The visual confirmation of the existence of weak non-covalent interactions among molecules of similar and dissimilar types was realized via NCIPLOT [29], a software tool specially designed for the visualization of such interactions based on the estimated ab initio electron density and its reduced electron density gradient upon interaction. Weak noncovalent interactions are therein represented with green isosurfaces, whereas strong attractive (repulsive) interactions are depicted with blue (red) isosurfaces, respectively.

Table S6: Computed shape descriptors for the three simulated systems

System #	λx [Å2]	λy [Å2]	λz [Å2]	*b* [Å2]	*k* [-]
1	461.7	494.5	597.9	119.9	6.3 x 10-3
2	465.4	486.4	578.9	103.0	4.7 x 10-3
3	542.2	550.6	553.7	7.3	4.0 x 10-5

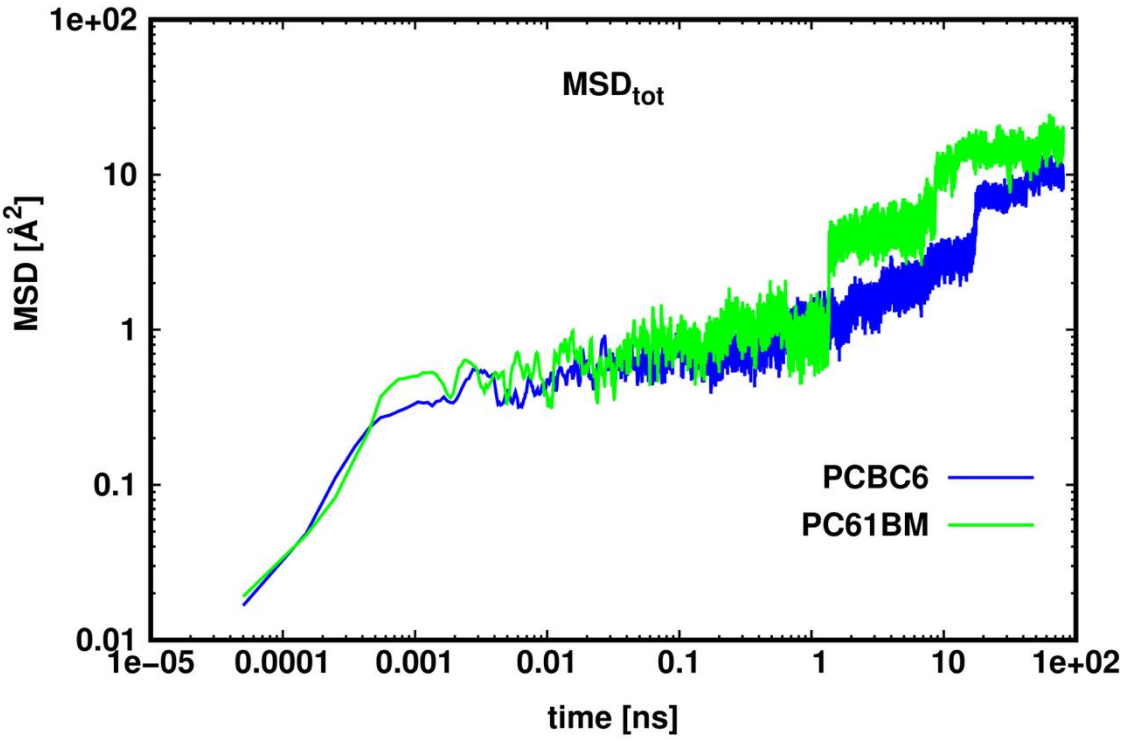

Figure S11. Mean square displacement (MSD) as a function of time for the center of mass of all PCBC6 and $PC_{61}BM$ molecules in systems 2 and 3, respectively.

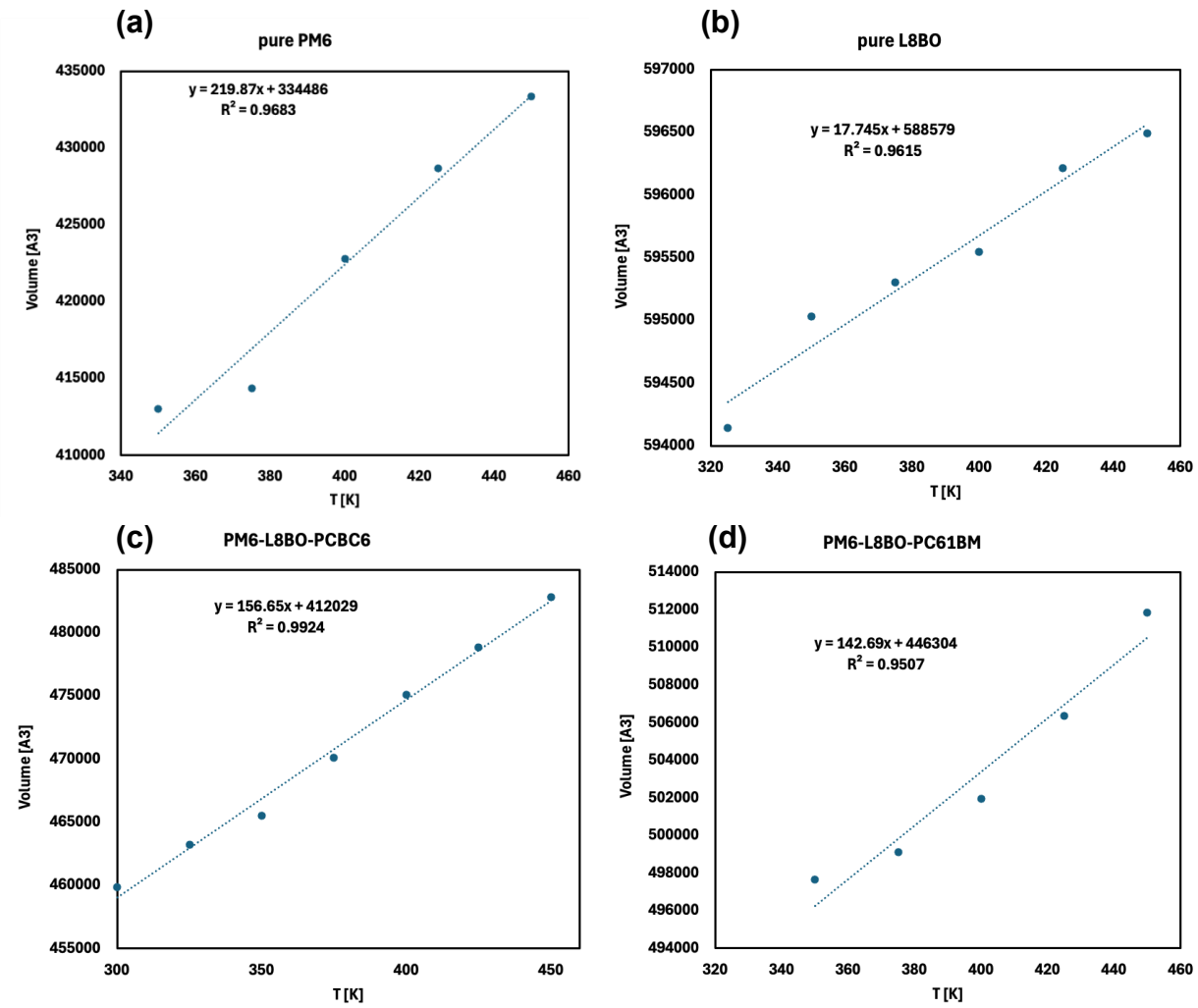

Figure S12**.** Computed equilibrium system's volume versus temperature for the estimation of the volumetric thermal expansion coefficient via Eq. S1 for (a) pure PM6, (b) pure L8-BO, (c) system 2 and (d) system 3 (see main text for details).

Supplementary Note 1

Sector integration of the in-plane and out-of-plane regions was performed using the regions highlighted in Supplementary Figure 1, using an azimuthal width of 30º, and 60º respectively for each region.

The peaks shown in Figure 2(d) were fitted using Pseudo-Voigt functions [30]. The crystal coherence length (CCL) was defined using the Scherrer equation as CCL = K × (2π/FWHM) (Å), where FWHM is the full width at half maximum of the corresponding diffraction peak, and K is the shape factor for the crystallite shape, where K = 0.9 is used here (approximately 0.89 – 0.93 is typically used for spherical crystallites) [31,32]. The fitted parameters are shown in Table.

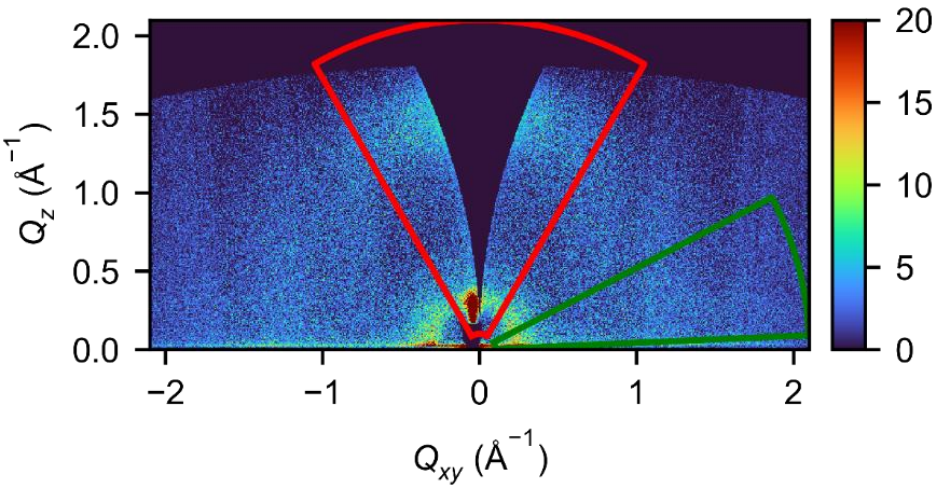

Figure S13: Visualisation of sector regions used for in-plane (green) and out-of-plane (red) line cuts.

Fitting results of the peaks shown in Figure 3d, where the lamellar and π-π peaks arise from the in-plane and out-of-plane integrations, respectively. η represents the Pseudo-Voigt mixing parameter between the Gaussian and Lorentzian fits, where η=0 would represent a pure Gaussian function.

		Q (Å-1)	d (Å)	FWHM (Å^{-1})	η	CCL (Å)
PM6:L8BO	**Lamellar**	0.303	20.706	0.107 (0.005)	0.564	52.8
	π-π	1.566	4.012	0.434 (0.002)	0.452	13.03
PM6:L8BO: PCBM	**Lamellar**	0.304	20.656	0.105 (0.005)	0.664	53.95
	π-π	1.570	4.004	0.434 (0.002)	0.478	13.03
PM6:L8BO: PCBC6	**Lamellar**	0.258	24.337	0.085 (0.005)	0.923	66.50
	π-π	1.556	4.038	0.416 (0.002)	0.303	13.59

References

1 W. S. Koh, M. Pant, Y. A. Akimov, W. P. Goh and Y. Li, *IEEE J Photovolt*, 2011, **1**, 84–92.

2 S. Zandi and M. Razaghi, *Solar Energy*, 2019, **179**, 298–306.

3 X. Li, Q. Zhang, J. Yu, Y. Xu, R. Zhang, C. Wang, H. Zhang, S. Fabiano, X. Liu, J. Hou, F. Gao and M. Fahlman, *Nature Communications 2022 13:1*, 2022, **13**, 1–9.

4 L. Zhu, M. Zhang, J. Xu, C. Li, J. Yan, G. Zhou, W. Zhong, T. Hao, J. Song, X. Xue, Z. Zhou, R. Zeng, H. Zhu, C. C. Chen, R. C. I. MacKenzie, Y. Zou, J. Nelson, Y. Zhang, Y. Sun and F. Liu, *Nat Mater*, 2022, **21**, 656–663.

5 T. Kirchartz, T. Agostinelli, M. Campoy-Quiles, W. Gong and J. Nelson, *Journal of Physical Chemistry Letters*, 2012, **3**, 3470–3475.

6 J. Larsson, *Am J Phys*, 2007, **75**, 230–239.

7 Y. Lin, Y. Firdaus, F. H. Isikgor, M. I. Nugraha, E. Yengel, G. T. Harrison, R. Hallani, A. El-Labban, H. Faber, C. Ma, X. Zheng, A. Subbiah, C. T. Howells, O. M. Bakr, I. McCulloch, S. De Wolf, L. Tsetseris and T. D. Anthopoulos, *ACS Energy Lett*, 2020, **5**, 2935–2944.

8 X. Zhao, R. Xia, H. Gu, H. Gu, X. Ke, Y. Shi, X. Chen, H. Jiang, H.-L. Yip, H.-L. Yip, S. Liu and S. Liu, *Optics Express, Vol. 28, Issue 2, pp. 2381-2397*, 2020, **28**, 2381–2397.

9 T. Ahmad, B. Wilk, E. Radicchi, R. Fuentes Pineda, P. Spinelli, J. Herterich, L. A. Castriotta, S. Dasgupta, E. Mosconi, F. De Angelis, M. Kohlstädt, U. Würfel, A. Di Carlo and K. Wojciechowski, *Adv Funct Mater*, 2020, **30**, 2004357.

10 C. J. Brabec, A. Cravino, D. Meissner, N. Serdar Sariciftci, T. Fromherz, M. T. Rispens, L. Sanchez and J. C. Hummelen, *Advanced Funtional Materials*, 2001, **11**, 374–380.

11 D. Luo, L. Zhang, L. Li, T. Dai, E. Zhou, M. Quan, H. Zhang, A. K. K. Kyaw and W. Y. Wong, *Advanced Science*, 2025, **12**, 2410154.

12 C. Gao, Y. Wang, H. Tian, K. Sun, C. Zhao, J. Che, S. Qiu, W. Chen, C. Huang, Z. Wang, H. Hu, P. Han, S. Li, Z. Luo and G. Zhang, *Advanced Materials*, 2025, e17576.

13 C. Zhang, X. Zhong, X. Sun, J. Lv, Y. Ji, J. Fu, C. Zhao, Y. Yao, G. Zhang, W. Deng, K. Wang, G. Li and H. Hu, *Advanced Science*, DOI:10.1002/ADVS.202401313.

14 Y. Cheng, B. Huang, Q. Mao, X. Huang, J. Liu, C. Zhou, W. Zhou, X. Ren, S. Kim, W. Kim, Z. Sun, F. Wu, C. Yang and L. Chen, *Advanced Materials*, DOI:10.1002/ADMA.202312938.

15 H. Chen, S. Y. Jeong, J. Tian, Y. Zhang, D. R. Naphade, M. Alsufyani, W. Zhang, S. Griggs, H. Hu, S. Barlow, H. Y. Woo, S. R. Marder, T. D. Anthopoulos, I. McCulloch and Y. Lin, *Energy Environ Sci*, 2023, **16**, 1062–1070.

16 F. Qi, Y. Li, R. Zhang, F. R. Lin, K. Liu, Q. Fan and A. K. Y. Jen, *Angewandte Chemie - International Edition*, 2023, **62**, e202303066.

17 R. Sun, Y. Wu, X. Yang, Y. Gao, Z. Chen, K. Li, J. Qiao, T. Wang, J. Guo, C. Liu, X. Hao, H. Zhu and J. Min, *Advanced Materials*, 2022, **34**, 2110147.

18 N. Gasparini, S. H. K. Paleti, J. Bertrandie, G. Cai, G. Zhang, A. Wadsworth, X. Lu, H. L. Yip, I. McCulloch and D. Baran, *ACS Energy Lett*, 2020, **5**, 1371–1379.

19 L. Martinez, R. Andrade, E. G. Birgin and J. M. Martínez, *J Comput Chem*, 2009, **30**, 2157–2164.

20 S. Plimpton, *J Comput Phys*, 1995, **117**, 1–19.

21 W. C. Swope, H. C. Andersen, P. H. Berens and K. R. Wilson, *J Chem Phys*, 1982, **76**, 637–649.

22 S. Nosé, *J Chem Phys*, 1984, **81**, 511–519.

23 W. G. Hoover, *Phys Rev A (Coll Park)*, 1985, **31**, 1695.

24 L. S. Dodda, I. C. De Vaca, J. Tirado-Rives and W. L. Jorgensen, *Nucleic Acids Res*, 2017, **45**, W331–W336.

25 H. A. Lorentz, *Ann Phys*, 1881, **248**, 127–136.

26 O. Buneman, *https://doi.org/10.1137/1025102*, 2006, **25**, 425–426.

27 C. L. Brooks, *Journal of Solution Chemistry 1989 18:1*, 1989, **18**, 99–99.

28 M. Doxastakis, Y. L. Chen, O. Guzmán and J. J. De Pablo, *J Chem Phys*, 2004, **120**, 9335–9342.

29 J. Contreras-García, E. R. Johnson, S. Keinan, R. Chaudret, J. P. Piquemal, D. N. Beratan and W. Yang, *J Chem Theory Comput*, 2011, **7**, 625–632.

30 F. Sánchez-Bajo and F. L. Cumbrera, *J Appl Crystallogr*, 1997, **30**, 427–430.

31 D. M. Smilgies, *urn:issn:0021-8898*, 2009, **42**, 1030–1034.

32 J. I. Langford and A. J. C. Wilson, *urn:issn:0021-8898*, 1978, **11**, 102–113.